Article

Effect of Ball Milling Parameters on the Refinement of Tungsten Powder

Zaoming Wu, Yanxia Liang, Engang Fu *, Jinlong Du, Peipei Wang, Yong Fan and Yunbiao Zhao

State Key Laboratory of Nuclear Physics and Technology, School of Physics, Peking University,
Beijing 100871, China; zmwu@pku.edu.cn (Z.W.); yxliang@pku.edu.cn (Y.L.); jldu@pku.edu.cn (J.D.);
ppwang@pku.edu.cn (P.W.); yfan1@pku.edu.cn (Y.F.); ybzhao1@pku.edu.cn (Y.Z.)

* Correspondence: efu@pku.edu.cn; Tel.: +86-10-6275-0612

check for updates

Abstract: The high-energy ball milling method was adopted to explore the influence of ball milling parameters, such as milling speed and additive amounts of process control agent (PCA) on tungsten powder. The morphology and microstructure of tungsten powder in the process of refinement were characterized by field-emission scanning electron microscope (FE-SEM), field-emission transmission electron microscope (FE-TEM), and X-ray diffractometer (XRD). Results revealed that the ball milling process and the refinement of tungsten particle and grain can be largely influenced by these two parameters. The milling efficiency was found to be highest with the milling speed of 700 rpm and additive amounts of 8% PCA. The mechanisms for the effect of these two parameters and milling time on the refinement process were discussed. Nanocrystalline tungsten powder with a particle size and grain size smaller than 100 nm was obtained, and the grain size of 5–15 nm was fabricated successfully under the highest milling efficiency conditions.

Keywords: morphology and microstructure; nanocrystalline tungsten; refinement; milling speed; process control agent

1. Introduction

Tungsten is one of the most promising plasma facing materials (PFMs) in fusion reactions due to its low thermal expansion coefficient, high melting point (3410 °C), low sputtering yield, good thermal conductivity, and high elevated temperature strength [1–3]. However, the disadvantages of tungsten [4–8], such as high ductile-to-brittle transition temperature (DBTT), low recrystallization temperature, and neutron radiation induced degradation, still restrict its application in fusion reactors. Therefore, it is necessary to improve these properties of tungsten to enable its application in harsh environments.

Recent research has shown that the refinement of tungsten grain size can improve its mechanical properties, such as the enhancement of its ductility [9–12]. Many methods have been proposed to refine the grain size, such as equal channel angular extrusion (ECAE) [13,14], high-pressure torsion (HPT) [15,16], accumulative roll bonding (ARB) [17,18], surface mechanical attrition treatment (SMAT) [19,20], and high-energy ball milling [21–26].

It is well known that high-energy ball milling is a mechanical milling process with a high level of deformation at a high strain rate. It is a simple, effective, and relatively low-cost method to synthesize nanostructured materials in the form of powder, which can be sintered to bulk samples. On the other hand, high-energy ball milling is also a very complex dynamic process that possesses plenty of variables, such as the ball to powder ratio (BPR), milling speed, additive amounts of process control agent (PCA), size and material of milling ball, milling time, filling ratio of mass, milling atmosphere, milling container, etc.

Ghayour et al. studied the effect of vial to plate spinning rate, ball size distribution, and type of balls on the performance of high-energy ball milling for the first time [27]. Suryanarayana reviewed the process and process variables involved in mechanical alloying (MA) and discussed the modeling of the MA process [28]. Oda et al. used the ball milling method to refine tungsten grain and obtained nano-grain with a diameter of approximately 10 nm. They defined the grain refinement process as a four-stage process [22,23]. Ameyama et al. adopted the MA process to ball mill W-10 wt % Re powder and they obtained nanoscale W-Re powder, which consists of a nano-grain structure with a grain size of 10–20 nm [21]. Both Oda and Ameyama selected a low milling speed of 200 rpm and small BPR (3.6:1 and 10:1) in their refinement process [21,22]. Zhao et al. used the MA method to ball mill W-3 wt % Y, and the grain size of tungsten was decreased from 1675 nm to 594 nm after 30 h of ball milling with a milling speed of 380 rpm [24]. Chen et al. used the MA method to refine the grain of W-15 wt % Nb alloy and obtained tungsten with a grain size of 28.3 nm when the rotation speed was 400 rpm [25]. Debata et al. used the MA method to ball mill the 95 W-3.5Ni-1.5Fe alloy for 15 h and obtained the minimum crystallite size of 18 nm with a milling speed of 300 rpm [26].

The studies show that nano/ultrafine-grained tungsten was obtained by adopting certain milling parameters. Many published articles on the same topics employed ball milling technology; however, many questions are still needed to be addressed for high-energy ball milling. A greater understanding of the effect of milling parameters during the refinement process of tungsten powder in ball milling treatment is still desired. For example, many existing references and researches paid close attention on the grain size of the milling powder, but neglected the particle size. Furthermore, detailed and systematic investigations of the relation between the evolution of microstructure and the refinement process are still lacking.

This manuscript gives a clear and intensive observation on the particle and grain refinement with different milling conditions. It is obvious that the higher the milling speed, the larger the energy input into the powder. However, the mechanisms through which the milling speed influences the refinement of tungsten powder are worth further investigation. The additive of PCA determines the grain size, grain shape, and purity of powder in final particles. It is vital to clarify the effect of additive amounts of PCA on the milling powder in the high-energy ball milling process. The milling time determines the particle and grain size, size distribution, shape, etc. It is necessary to investigate the refinement process of ball-milled powder based on the morphology and microstructure at different time periods. Meanwhile, this paper explores the optimal milling conditions required to obtain nanoscale tungsten powder based on the particle and grain refinement process.

2. Materials and Methods

Commercial pure tungsten powder with a particle size mostly smaller than 1 μm and a purity of 99.9% was used as the initial powder. The tungsten powder was mechanically alloyed in a Fritsch pulverisette 7 premium line planetary mill with a vessel made of zirconium oxide. The milling balls with a diameter of 1 mm were also made of zirconium oxide. To avoid the agglomeration and caking of tungsten powder ball-milled by dry milling, the wet milling method was utilized by adding ethanol as the PCA. Our milling vessels are suitable for different milling atmospheres (such as Ar, N_2, and H_2). These milling vessels are fully enclosed and no gas exchanges during the high-energy ball milling process as the vessels are sealed with a gas viton valve and a silicone flat sealing ring. Furthermore, the mass was measured to be the same for the vessels (containing tungsten powder and ethanol) before and after the ball milling process. The initial tungsten powder was ball-milled for total time of 60 h in purified N_2 gas (purity 99.999%). Table 1 shows the samples processed under different ball milling parameters including milling speed, PCA, and milling time. Five experiments with different milling speeds (samples 1, 2, and 3) and different additive amounts of PCA (samples 3, 4, and 5) were conducted.

**Table 1.** The ball milling parameters for different samples (PCA: process control agent).

Sample Number	Milling Speed (rpm)	PCA (%)	Total Milling Time (h)	D_{50} (nm) at 30 h Milling	D_{50} (nm) at 60 h Milling
1	300	8	60	1050	90
2	500	8	60	50	44
3	700	8	60	24	27
4	700	6	60	220	27
5	700	12	60	28	16

The ball-milled tungsten powder samples were taken into a centrifuge tube in a glove box filled with nitrogen. Then, the samples were ultrasonic dispersed for 40 min to make SEM samples and TEM samples. The morphology and powder refinement process were characterized by field-emission scanning electron microscope (FE-SEM; FEI Company, Hillsboro, OR, USA), transmission electron microscope (TEM; FEI Company, Hillsboro, OR, USA), and high resolution TEM (HRTEM; FEI Company, Hillsboro, OR, USA). The instrument model employed was FEI Nano SEM 430 and FEI Tecnai F30 TEM. The grain size information of the tungsten powder samples was characterized by X-ray diffraction (XRD; PANalytical Company, Almelo, The Netherlands), which was also used for the qualitative analysis of grain size information of ball-milled tungsten. The quantitative analysis of the grain size of ball-milled tungsten powder was obtained by the dark field (DF) TEM image. The software Nanomeasurer (1.2.5, J.X., Fudan University, Shanghai, China, 2008) was used on the SEM images to obtain the particle size distribution and medium particle size (D_{50}) of tungsten particles. In order to obtain the reliable distribution of the particle size, plenty of SEM images of each sample were randomly selected and the particle size was recorded on different positions. More than 1000 particles for each image were used to determine the Martin particle distribution and the particle size distribution, based on the number percentage.

3. Results and Discussion

3.1. Initial Tungsten Powder

Figure 1a and Figure S1 show that the initial tungsten powder has a polyhedron-type morphology and an equiaxed structure. Figure 1b of particle size distribution shows that the particle size presents nearly positive skewness distribution. The size of the initial tungsten particles is mostly smaller than 1 μm, and the medium size (D_{50}) of the particle is 450 nm. D_{50} is the corresponding particle size when a sample of the cumulative size distribution percentage reaches 50%. The XRD pattern in Figure 1c shows that the initial tungsten powder has body-centered cubic (bcc) structure with the α-W phase.
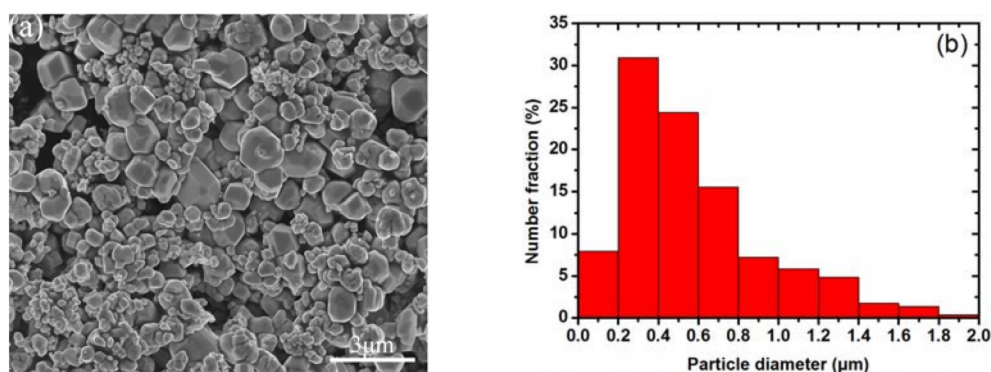

Figure 1. *Cont.*
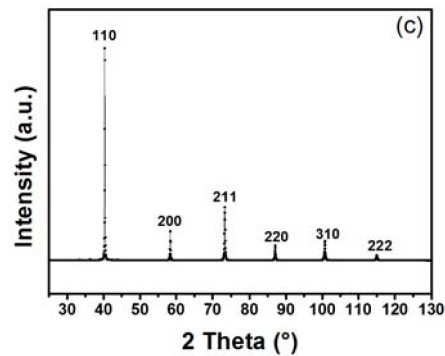
Figure 1. The initial tungsten powder: (**a**) SEM image; (**b**) the particle size distribution; (**c**) the X-ray diffraction (XRD) pattern.

3.2. The Effect of Milling Speed

Three samples (samples 1, 2, and 3 in Table 1) were ball-milled with a milling speed of 300 rpm, 500 rpm, and 700 rpm, respectively. They have the same BPR of 15:1 and a PCA of 8% (accounting for the total mass of the milling ball and tungsten powder). Figure 2 shows the SEM images of tungsten ball-milled with a milling speed of 300 rpm, 500 rpm, and 700 rpm, respectively. The milling time was 30 h and 60 h for each milling speed. Figure 3 shows the corresponding particle size distributions for these samples.
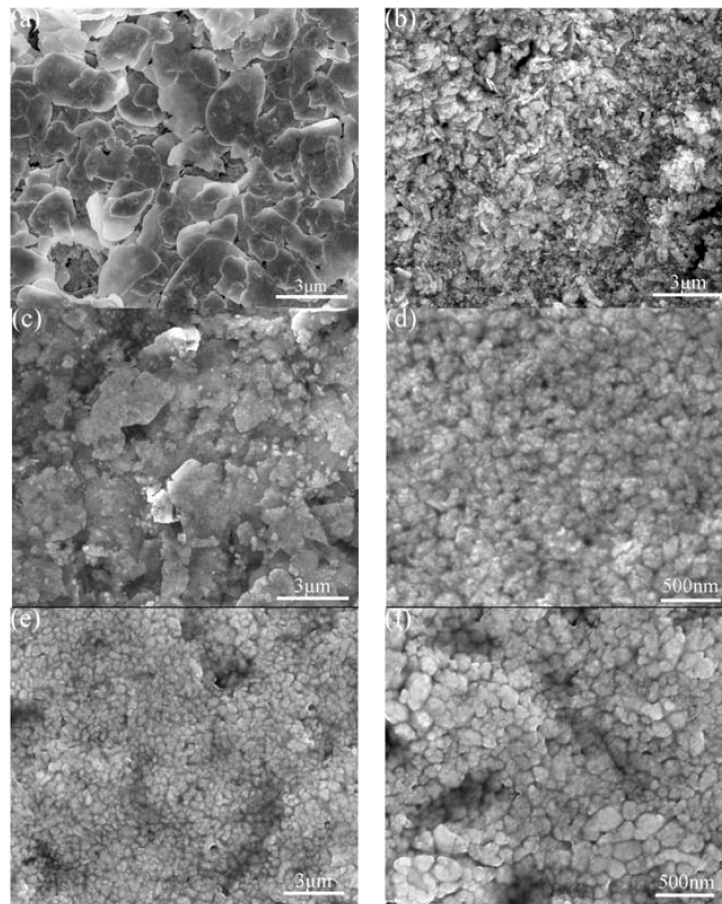
Figure 2. The SEM images of ball-milled tungsten powder at different milling time with different milling speeds: (**a**) 300 rpm, 30 h; (**b**) 300 rpm, 60 h; (**c**) 500 rpm, 30 h; (**d**) 500 rpm, 60 h; (**e**) 700 rpm, 30 h; (**f**) 700 rpm, 60 h.
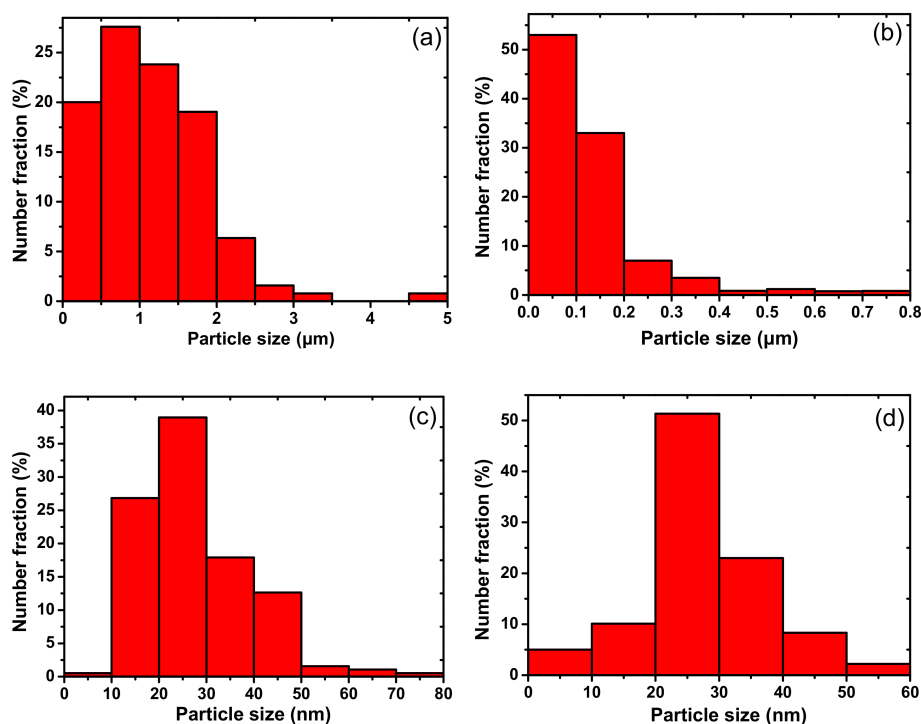
Figure 3. The particle size distribution of ball-milled tungsten with different milling speeds at different milling time: (**a**) 300 rpm, 30 h; (**b**) 300 rpm, 60 h; (**c**) 700 rpm, 30 h; (**d**) 700 rpm, 60 h.

When the milling speed was 300 rpm, Figure 2a shows that the particle of tungsten ball-milled at 30 h has a flake structure. Most particle sizes are in the micron-scale, as shown in Figure 3a, and the D_{50} of the tungsten particles is 1050 nm. Few nanoscale particles fall off from the micron-scale particles with a flake structure, which means that the ball-milled tungsten powder is in the squeezing stage [29]. As the milling time increases, the micron-scale particles with the flake structure are further squeezed, and finally the particles are smashed and fractured. Figure 2b is SEM image of tungsten powder ball-milled with a milling speed of 300 rpm after 60 h, and shows large amount of nanoscale particles. The D_{50} of the tungsten particles is 90 nm. Figure 3b shows the particle size distribution of tungsten powder ball-milled at 60 h, and the tungsten powder with a size of several hundred nanometer particles still exists.

When the milling speed increases to 500 rpm, Figure 2c shows that the tungsten powder appears in a flake structure in the micron-scale, and large amount of particles are in the nanoscale after 30 h of ball milling. The size of tungsten particles is in the range from the nanoscale to micron-scale with a D_{50} of 50 nm, as shown in Reference [29]. The ball-milled tungsten powder is in the fracturing stage [29], and a large amount of nanoscale particles appear. When the milling time increases to 60 h, the micron-scale particles are further refined and disappear gradually, as shown in Figure 2d. The D_{50} of the tungsten particles is 50 nm, as shown in Reference [29], which gives the particle size distribution.

When the milling speed is 700 rpm, Figure 2e shows that the tungsten powder particles exhibit serious agglomeration. The refinement process is very fast, and the tungsten particles are fractured into a nanoscale size after 30 h of ball milling, with a D_{50} of 24 nm as shown in Figure 3c, depicting the particle size distribution. When the milling time increases to 60 h, the tungsten particles also exhibit serious agglomeration, as shown in Figure 2f and Figure S2 depicting the tungsten powder ball-milled for 60 h. Figure 3d, depicting the particle size distribution, shows that the particle size of tungsten powder is less than 50 nm with a D_{50} of 27 nm.

Figure 4 shows the bright field (BF) and DF TEM images of tungsten powder ball-milled with a milling speed of 300 rpm, 500 rpm, and 700 rpm at 60 h. Figure 4a is the BF TEM image of tungsten
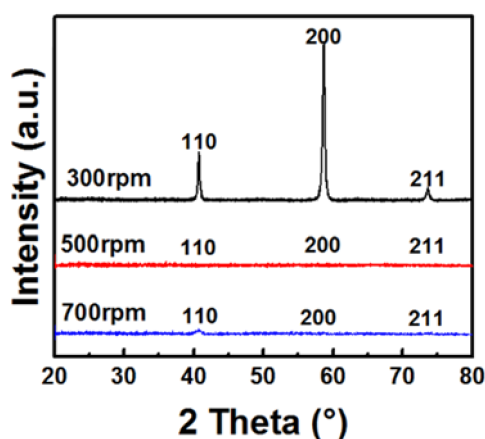
powder ball-milled with a milling speed of 300 rpm at 60 h, and shows that the particle size is in the micron-scale, and the corresponding selected area electron diffraction (SAED) image shows that the SAED spots are discrete (non-nanocrystalline tungsten). This means that no nanocrystalline tungsten is formed after 60 h of ball milling at 300 rpm. Also, the corresponding DF image of Figure 4b shows that the grain size is in the hundred nanometer-scale, and the white areas are the grains in the (110) crystal direction, which satisfies the diffraction condition. Every particle possesses several grains or more. The nanometric particle size was obtained from the statistic particle size of SEM images. The grain size was obtained from the dark-field (DF) TEM image of tungsten powder. We chose one diffraction spot in the (110) crystal direction and entangled this point with the aperture of an objective lens to obtain the dark-field TEM image and grain size.
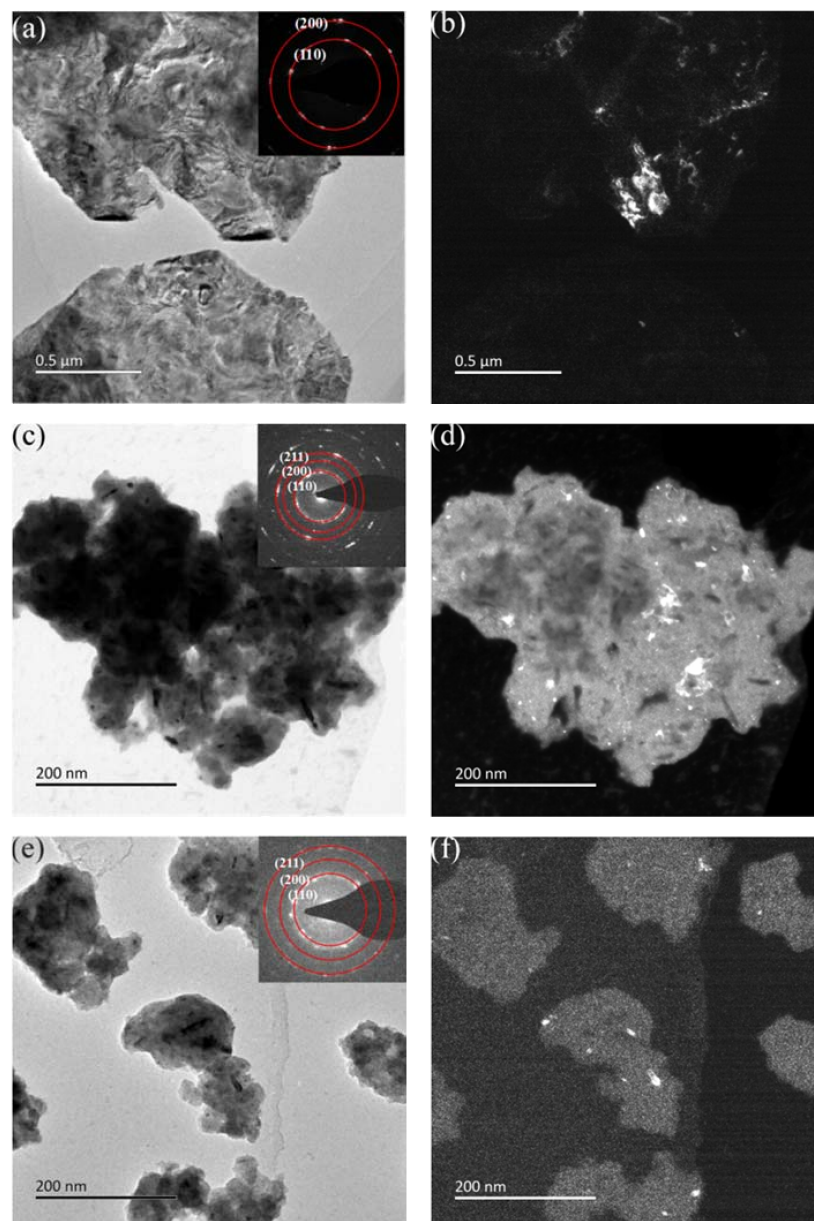
Figure 4. The TEM images of ball-milled tungsten powder with 8% process control agent (PCA) and different milling speeds. (**a**) 300 rpm, 60 h, BF TEM image; (**b**) 300 rpm, 60 h, DF TEM image; (**c**) 500 rpm, 60 h, BF TEM image; (**d**) 500 rpm, 60 h, DF TEM image; (**e**) 700 rpm, 60 h, BF TEM image; (**f**) 700 rpm, 60 h, DF TEM image.

Figure 4c is the BF TEM image of tungsten powder ball-milled with a milling speed 500 rpm at 60 h, and shows that the particle size is in the nanometer scale. The corresponding SAED image shows that the SAED spots are concentric circles with dense or continuous spots in one concentric circle (nanocrystalline tungsten). This indicates the formation of nanocrystalline tungsten. Moreover, the DF TEM image in Figure 4d shows that the grain size ranges from 5 nm to 25 nm. Figure 4e is the BF TEM image of tungsten powder ball-milled with a milling speed of 700 rpm at 60 h, and shows that the particle size ranges from 32 nm to 160 nm. The corresponding SAED image reveals the formation of nanocrystalline tungsten and the DF TEM image in Figure 4f shows that the grain size ranges from 5 nm to 15 nm. All SAED patterns of tungsten powder given in this work indicate that the tungsten powder has a polycrystalline structure. The nanocrystalline powder is also a polycrystalline powder; the difference is that it has nanocrystalline grain. The SAED spots of nanocrystalline tungsten powder are concentric circles with dense or continuous spots in one concentric circle, while the SAED spots are discrete spots of non-nanocrystalline tungsten powder.

Figure 5 shows the X-ray diffraction (XRD) patterns of tungsten powder ball-milled with different milling speeds after 60 h. The results show that the full width at half maxima (FWHM) of Bragg peaks of (110), (200), and (211) from tungsten powder ball-milled with 300 rpm after 60 h is the smallest, indicating that its grain size is the largest among the samples. As the FWHM of the corresponding peaks from the samples with milling speeds of 500 rpm and 700 rpm is nearly the same, their grain size after 60 h of ball milling is very close. The XRD patterns show the disappearance or the broadening of Bragg peaks of (200) and (211) in ball-milled tungsten powder milled at speeds 500 rpm and 700 rpm, which indicates the formation of small grains with a size of several nanometers, as illustrated in Figure 4d,f, as well as the existence of large amounts of lattice strain.

Figure 5. The XRD pattern at 60 h ball-milled tungsten powder with different milling speeds.

Samples 1, 2, and 3 are the tungsten powder ball-milled at different milling speeds. After comparing the tungsten powder ball-milled for the same milling time with different milling speeds, our conclusions can be summarized as follows: the milling speed has a significant influence on the refinement process, and the larger the milling speed, the faster the refinement process. This results in the ball-milled tungsten powder exhibiting different refinement stages after the same milling time. Therefore, the tungsten powder shows different morphologies and microstructures under different milling speeds. The particle size and grain size of ball-milled tungsten decrease with the increase of the milling speed. Tungsten powder subjected to milling speeds of 500 rpm and 700 rpm for 60 h of milling time exhibits feature of nanoscale particles. As the milling speed increases, the speed of the milling balls in the milling vessel increases, and the average mean free distance of single powder colliding to ball decreases. Thus, the collision frequency with the tungsten powder increases, since the size of the vessel is fixed.

Under the same milling conditions, the total energy consumed for ball milling is equal to the energy provided by the planetary mill expressed by $E_{mill} = \kappa\omega^3 t$ [30], where κ is a constant related to the given mill, ω is the angular speed of the mill rotation, and t is the milling time. Thus, the energy provided by high-energy ball milling is in direct cubic proportion to the angular speed. If the rotate speed is increased, the energy provided by the planetary mill increases. That is to say, the energy consumed for each powder increases, and this energy determines the stress that applies to tungsten powder and influences the particle size and grain size of ball-milled tungsten powder. So, a higher milling speed will speed up the refinement process and reduce the milling time required to obtain a certain particle and grain size.

3.3. The Effect of Additive Amounts of Process Control Agent (PCA)

Three samples (samples 3, 4, and 5 in Table 1) ball-milled with PCAs of 8%, 6%, and 12% were compared to investigate the effect of the PCA on the refinement process. The other parameters of ball milling were maintained the same: a milling speed of 700 rpm and a BPR of 15:1.

Figure 6 shows the SEM images of tungsten powder ball-milled at 30 h and 60 h with different PCAs of 6% and 12%. Figure 6a shows the tungsten powder ball-milled for 30 h with a PCA of 6%, and the tungsten particles appear to have a flake structure. Figure 7a shows that the corresponding size of tungsten particles is mostly in the range of several hundred nanometers, and the D_{50} of particle size is 220 nm. With the increase of milling time to 60 h, Figure 6b shows that the tungsten powder is further refined, and the particles are smashed and fractured. The particles exhibit serious agglomeration. Most of tungsten particle sizes are in the nanoscale, as shown in Figure 7b depicting particle size distribution, and the D_{50} of particle size is 27 nm.
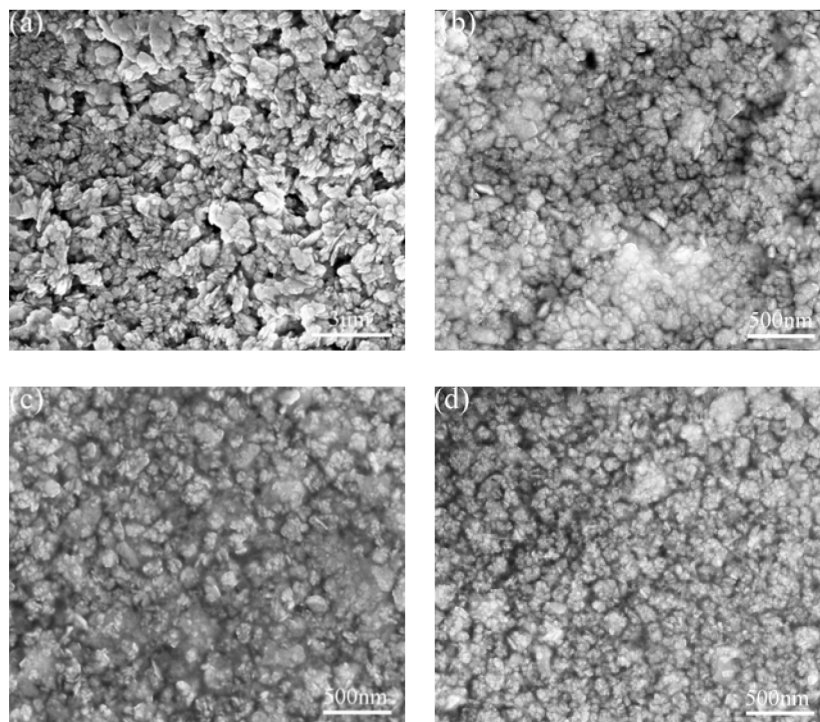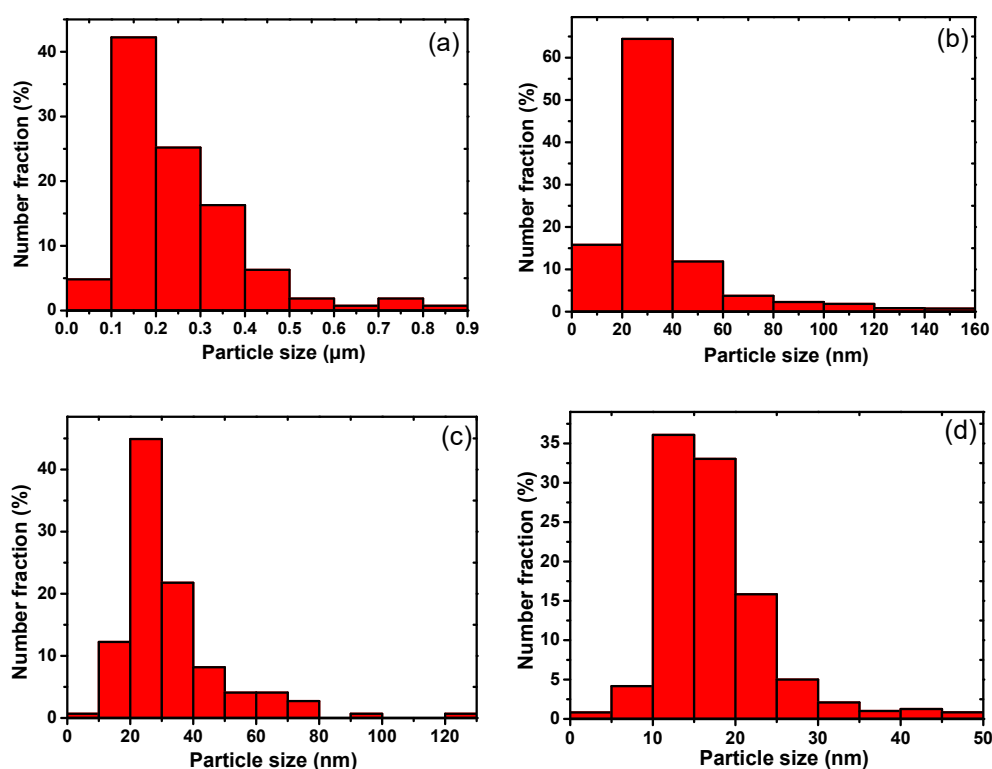

Figure 6. The SEM images of ball-milled tungsten at different milling time with different additive amounts of PCA: (**a**) 6% PCA, 30 h; (**b**) 6% PCA, 60 h; (**c**) 12% PCA, 30 h; (**d**) 12% PCA, 60 h.

When the PCA is 12% and the milling time is 30 h, Figure 6c reveals a small amount of flake structure particles with a particle size of about 100 nm, and the particles exhibit serious agglomeration. Figure 7c shows that the powder particle size is mostly in the nanoscale, and the D_{50} of particle size

is 28 nm. With the increase of milling time, the particle size is further reduced and some particles agglomerate to form a large particle with a size of about hundred nanometers, as shown in Figure 6d. The particle size is mostly less than 30 nm and the D_{50} of particle size is 16 nm, as shown in Figure 7d depicting the particle size distribution.

Figure 8 shows the BF and DF TEM images of tungsten powder ball-milled at 60 h with the additive amounts of PCA of 6% and 12%. The TEM images with the additive amounts of 8% PCA are already shown in Figure 4e,f. Figure 8a is the BF TEM image of tungsten powder ball-milled at 60 h with the additive amount of 6% PCA, and shows that the particle size ranges from 24 nm to 280 nm. The particle size is not uniform. The corresponding SAED image reveals the formation of nanocrystalline tungsten and the DF image of Figure 8b shows that the grain size ranges from 5 nm to 36 nm. Figure 8c is the BF image of tungsten powder ball-milled at 60 h with the additive amount of 12% PCA, which shows that the particle size ranges from 9 nm to 108 nm. The corresponding SAED image reveals the formation of nanocrystalline tungsten, and the DF TEM image of Figure 8d shows that the grain size ranges from 5 nm to 20 nm.


Figure 7. The particle size distribution of ball-milled tungsten at different milling time with different additive amounts of PCA: (**a**) 6% PCA, 30 h; (**b**) 6% PCA, 60 h; (**c**) 12% PCA, 30 h; (**d**) 12% PCA, 60 h.

Figure 9 shows the XRD patterns of tungsten powder after 60 h of ball milling with different additive amounts of PCA. The results reveal that the additive amount of PCA has a great influence on the grain size of ball-milled tungsten powder. The FWHM of Bragg peaks from planes of (110), (200), and (211) in the XRD pattern of tungsten powder with 8% PCA is larger than that with 6% or 12% PCA. This indicates that its grain size is the smallest, as illustrated by Figures 4f and 8b,d. Moreover, the lattice strain is largest among these three samples.
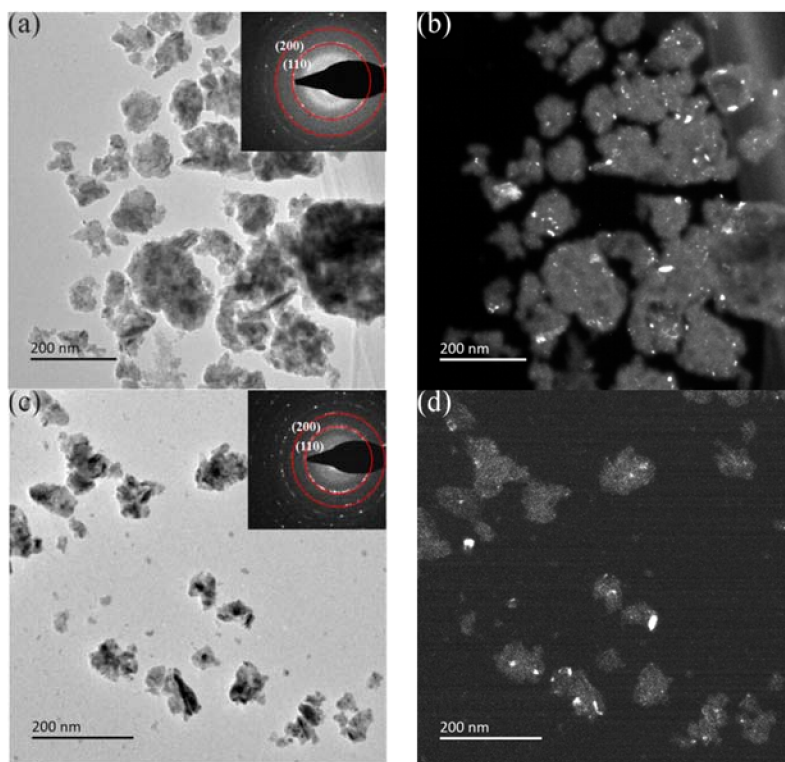
Figure 8. The TEM images of ball-milled tungsten powder with different additive amounts of PCA. (**a**) 6% PCA, 700 rpm, 60 h, BF TEM image; (**b**) 6% PCA, 700 rpm, 60 h, DF TEM image; (**c**) 12% PCA, 700 rpm, 60 h, BF TEM image; (**d**) 12% PCA, 500 rpm, 60 h, DF TEM image.
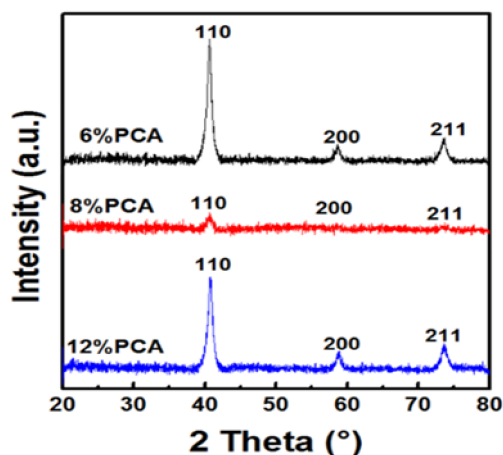
Figure 9. The XRD pattern of tungsten powder ball-milled for 60 h with different additive amounts of PCA.

Samples 3, 4, and 5 are the tungsten powder ball-milled with different additive amounts of PCA. The SEM images in Figure 2e,f and Figure 6 show that when the additive amount of PCA is 8%, the efficiency of ball milling is highest. The efficiency of tungsten powder with 12% PCA is higher than that of 6% PCA. This fact indicates that the additive amount of PCA plays a significant role in the milling process.

In the milling process, the powder is subjected to serious plastic deformation, and cold welding occurs between the tungsten particles. This would impede the further fracturing of tungsten powder, and the addition of PCA could minimize the cold welding and the caking through the adherence of the

powder's surfaces. The PCA acts as surface-active agent to ensure that every single tungsten particle is impacted uniformly, and improves the efficiency of high-energy ball milling. The PCA adheres to the surface of tungsten powder, and this may reduce the energy (E) required for the physical process of size reduction. The energy of E is given by $E = \gamma * \Delta S$, where γ refers to the specific surface energy and ΔS is the increase of the surface area in the milling process. The addition of PCA could lower the surface tension of ball-milled tungsten powder. Thus, it could reduce the surface energy, and would reduce the milling time required to refine the tungsten particles.

In comparison to the particles with moderate additive amounts of PCA, the lower additive amounts of PCA result in the inhomogeneous distribution of PCA. Consequently, the particles are impacted unevenly. Excess additive amounts of PCA result in the viscous resistance of milling balls. This reduces the velocity of milling ball directly, and thus reduces the frequency of collisions and the energy transferred to tungsten powder. As a result, the milling efficiency is reduced. The additive amounts of moderate PCA improve the milling efficiency significantly, and could decrease the milling time to obtain nanoscale uniform-sized tungsten particles and improve the formation process of small tungsten grain with a size of several nanometers.

4. Conclusions

High-energy ball milling experiments with different milling speeds and different additive amounts of PCA were conducted on tungsten powder. A detailed and systematic investigation of the relation between the evolution of microstructure and the refinement process was conducted. The influences of ball milling parameters on tungsten powder were studied carefully. A comparison of the ball-milled tungsten with different milling speeds showed that the milling efficiency is the highest with a milling speed of 700 rpm and 8% PCA. The milling efficiency can be improved by increasing the milling speed and adding appropriate additive amounts of PCA. The mechanisms for the effect of milling speed and amount of PCA on the morphology and microstructure of tungsten particle and grain were described. Nanocrystalline tungsten powder with a particle size and grain size smaller than 100 nm was obtained, and the grain size of 5–15 nm was fabricated successfully.

Author Contributions: Z.W. and Y.L. contributed equally to the work. Z.W., Y.L. and E.F. conceived and designed the experiments; Z.W. and Y.L. performed the experiments and analyzed the data; Z.W. and E.F. wrote the paper and discussed with Y.L., Y.F. and Y.Z.; J.D. and P.W. contributed reagents/materials/analysis tools.

Conflicts of Interest: The authors declare no conflict of interest.

References

1. Davis, J.W.; Barabash, V.R.; Makhankov, A.; Plochl, L.; Slattery, K.T. Assessment of tungsten for use in the ITER plasma facing components. *J. Nucl. Mater.* **1998**, *258–263*, 308–312. [CrossRef]
2. Norajitra, P.; Boccaccini, L.V.; Diegele, E.; Filatov, V.; Gervash, A.; Giniyatulin, R.; Gordeev, S.; Heinzel, V.; Janeschitz, G.; Konys, J.; et al. Development of a helium-cooled divertor concept: Design-related requirements on materials and fabrication technology. *J. Nucl. Mater.* **2004**, *329–333*, 1594–1598. [CrossRef]
3. Petti, D.A.; McCarthy, K.A.; Gulden, W.; Piet, S.J.; Seki, Y.; Kolbasov, B. An overview of safety and environmental considerations in the selection of materials for fusion facilities. *J. Nucl. Mater.* **1996**, *233–237*, 37–43. [CrossRef]
4. Smid, I.; Akiba, M.; Diegele, E.; Vieider, G.; Plochl, L. Development of tungsten armor and bonding to copper for plasma-interactive components. *J. Nucl. Mater.* **1998**, *253–263*, 160–172. [CrossRef]

5.   Philipps, V. Tungsten as material for plasma-facing components in fusion devices. *J. Nucl. Mater.* **2011**, *415*, S2–S9. [CrossRef]

6.   Linke, J. Plasma facing materials and components for future fusion devices—Development, characterization and performance under fusion specific loading conditions. *Phys. Scr.* **2006**, *123*, 45–53. [CrossRef]

7.   Singheiser, L.; Hirai, T.; Linke, J.; Pintsuk, G.; Rödig, M. Plasma-facing materials for thermo-nuclear fusion devices. *Trans. Indian Inst. Met.* **2009**, *62*, 123–128. [CrossRef]

8.   Mathaudhu, S.N.; de Rosset, A.J.; Hartwig, K.T.; Kecskes, L.J. Microstructures and recrystallization behavior of severely hot-deformed tungsten. *Mater. Sci. Eng. A* **2009**, *503*, 28–31. [CrossRef]

9.   Senthilnathan, N.; Annamalaia, A.R.; Venkatachalam, G. Microstructure and mechanical properties of spark plasma sintered tungsten heavy alloys. *Mater. Sci. Eng. A* **2018**, *710*, 66–73. [CrossRef]

10. Xie, Z.M.; Miao, S.; Zhang, T.; Liu, R.; Wang, X.P.; Fang, Q.F.; Hao, T.; Zhuang, Z.; Liu, C.S.; Lian, Y.Y.; et al. Recrystallization behavior and thermal shock resistance of the W-1.0 wt % TaC alloy. *J. Nucl. Mater.* **2018**, *501*, 282–292. [CrossRef]

11. Li, X.B.; Zhu, D.H.; Li, C.J.; Chen, J.L. Cracking and grain refining behaviors of tungsten based plasma facing materials under fusion relevant transient heat flux. *Fusion Eng. Des.* **2017**, *125*, 515–520. [CrossRef]

12. Xiao, F.N.; Xu, L.J.; Zhou, Y.C.; Pan, K.M.; Li, J.W.; Liu, W.; Wei, S.Z. Preparation, microstructure, and properties of tungsten alloys reinforced by ZrO$_2$ particles. *Int. J. Refract. Met. Hard Mater.* **2017**, *64*, 40–46. [CrossRef]

13. Chen, W.G.; Feng, P.; Dong, L.L.; Liu, B.; Ren, S.X.; Fu, Y.Q. Experimental and theoretical analysis of microstructural evolution and deformation behaviors of CuW composites during equal channel angular pressing. *Mater. Des.* **2018**, *142*, 166–176. [CrossRef]

14. Hester, M.W.; Usher, J.M. Recycling welding rod residuals based on development of a top-down nanomanufacturing system employing indexing equal channel angular pressing. *Int. J. Adv. Manuf. Technol.* **2018**, *94*, 1087–1099. [CrossRef]

15. Edalati, K.; Hashiguchi, Y.; Pereira, P.H.R.; Horita, Z.; Langdon, T.G. Effect of temperature rise on microstructural evolution during high-pressure torsion. *Mater. Sci. Eng. A* **2018**, *714*, 167–171. [CrossRef]

16. Bazarnik, B.; Huang, Y.; Lewandowska, M.; Langdon, T.G. Enhanced grain refinement and microhardness by hybrid processing using hydrostatic extrusion and high-pressure torsion. *Mater. Sci. Eng. A* **2018**, *712*, 513–520. [CrossRef]

17. Fattah-alhosseini, A.; Reza Ansari, A.; Mazaheri, Y.; Karimi, M.; Haghshenas, M. An Investigation of mechanical properties in accumulative roll bonded nano-grained pure titanium. *Mater. Sci. Eng. A* **2017**, *688*, 218–224.

18. Fattah-alhosseini, A.; Keshavarz, M.K.; Mazaheri, Y.; Reza Ansari, A.; Karimi, M. Strengthening mechanisms of nano-grained commercial pure titanium processed by accumulative roll bonding. *Mater. Sci. Eng. A* **2017**, *693*, 164–169.

19. Bahl, S.; Suwas, S.; Ungàr, T.; Chatterjee, K. Elucidating microstructural evolution and strengthening mechanisms in nanocrystalline surface induced by surface mechanical attrition treatment of stainless steel. *Acta Mater.* **2017**, *122*, 138–151.

20. Tsai, M.T.; Huang, J.C.; Tsai, W.Y.; Chou, T.H.; Chen, C.F.; Li, T.H.; Jang, J.S.C. Effects of ultrasonic surface mechanical attrition treatment on microstructures and mechanical properties of high entropy alloys. *Intermetallics* **2018**, *93*, 113–121. [CrossRef]

21. Ameyama, K.; Oda, E.; Fujiwara, H. Superplasticity and high temperature deformation behaviour in nano grain tungsten compacts. *Materialwiss. Werkstofftech.* **2008**, *39*, 336–339. [CrossRef]

22. Oda, E.; Fujiwara, H.; Ameyama, K. Nano grain formation in tungsten by severe plastic deformation-mechanical milling process. *Mater. Trans.* **2008**, *49*, 54–57. [CrossRef]

23. Oda, E.; Ameyama, K.; Yamaguchi, S. Fabrication of nano grain tungsten compact by mechanical milling process and its high temperature properties. *Mater. Sci. Forum* **2006**, *503–504*, 573–578. [CrossRef]

24. Zhao, M.; Zhou, Z.; Tan, J.; Ding, Q.; Zhong, M. Effects of ball milling parameters on microstructural evolution and mechanical properties of W–3% Y composites. *J. Nucl. Mater.* **2015**, *465*, 6–12. [CrossRef]

25. Chen, J.; Luo, L.; Lin, J.; Zan, X.; Zhu, X.; Luo, G.; Wu, Y. Influence of ball milling processing on the microstructure and characteristic of W-Nb alloy. *J. Alloys Compd.* **2017**, *694*, 905–913. [CrossRef]

26. Debata, M.; Acharya, T.S.; Sengupta, P.; Acharya, P.P.; Baipai, S.; Jayasankkar, K. Effect of high energy ball milling on structure and properties of 95W-3.5Ni-1.5Fe heavy alloys. *Int. J. Refract. Met. Hard Mater.* **2017**, *69*, 170–179. [CrossRef]

27. Ghayour, H.; Abdellahi, M.; Bahmanpour, M. Optimization of the high energy ball-milling: Modeling and parametric study. *Power Technol.* **2016**, *291*, 7–13. [CrossRef]

28. Suryanarayana, C. Mechanical alloying and milling. *Prog. Mater. Sci.* **2001**, *46*, 11–84. [CrossRef]

29. Liang, Y.X.; Wu, Z.M.; Fu, E.G.; Du, J.L.; Wang, P.P.; Zhao, Y.B.; Qiu, Y.H.; Hu, Z.Y. Refinement process and mechanisms of tungsten powder by high energy ball milling. *Int. J. Refract. Met. Hard Mater.* **2017**, *67*, 1–8. [CrossRef]

30. Kurlov, A.S.; Gusev, A.I. Model for milling of powders. *Tech. Phys.* **2011**, *56*, 975–980. [CrossRef]